



GEORG-AUGUST-UNIVERSITÄT
GÖTTINGEN

Fakultät für
Physik

Intermediate Report for Master's Project

$t\bar{t}(H \rightarrow WW^*)$ Rekonstruktion mit Neutrino Gewichtung & SPA-Net

$t\bar{t}(H \rightarrow WW^*)$ event reconstruction techniques using neutrino-weighting & SPA-Net

prepared by

Ireas Tom Raschke

from Finsterwalde

at the II. Physikalisches Institut

Module number: M.Phy.408: Research Lab Course in Nuclear and Particle Physics

Period: 3rd November 2023 until 3rd October 2024

Referee: Prof. Dr. Arnulf Quadt

Contents

1	Introduction	3
2	The Standard Model of Particle Physics	5
2.1	Gauge Symmetry and Spontaneous Symmetry Breaking	5
2.2	Particles	6
2.2.1	Fermions	6
2.2.2	Bosons	9
2.3	Beyond the Standard Model	11
2.4	Higgs-Associated Top Quark Pair Production	12
3	Experimental Setup	15
3.1	Large Hadron Collider	15
3.2	The ATLAS Experiment	16
3.2.1	Detector	17
3.2.2	Coordinate System	21
3.3	Other Experiments	21
4	Methods	25
4.1	SPA-Net	25
4.2	Truth Matching	27
4.3	Neutrino Weighting	27
5	Current Status	31
5.1	Truth Matching	31
5.1.1	Truth Matching Algorithm	31
5.1.2	Successful Event Matches	32
5.1.3	Final Jet Selection	33
5.1.4	Higgs Decay Modes	33
5.2	NAF Computing Grid	34
6	Outlook	37

TODO UPDATE REFERENCES

1 Introduction

TODO EXPAND ON THE INTRODUCTION - AFTER HISTORIC SAME CONCRETE THINGS ABOUT LHC AND ATLAS IN CONTEXT OF SM: GIVE BRIEF OVERVIEW OVER WHICH TOPICS THE INDIVIDUAL SECTION OF REPORT WILL COVER!

2 The Standard Model of Particle Physics

The Standard Model of particle physics (SM) stands as the most successful framework in understanding the fundamental particles and their interactions to date. It encompasses all known elementary particles along with their antiparticles, and three out of the four known fundamental forces: the strong, weak, and electromagnetic forces. Notably, gravity remains beyond the scope of the SM.

2.1 Gauge Symmetry and Spontaneous Symmetry Breaking

The SM is a renormalisable quantum field theory [1, 2] characterised by an internal gauge symmetry that is denoted as a $SU(3)_C \otimes SU(2)_L \otimes U(1)_Y$. A gauge symmetry describes the fundamental principle of the invariance of physical systems under certain transformations associated with the corresponding gauge field [3].

The $SU(3)_C$ group symmetry describes the strong interaction, stemming from quantum chromodynamics (QCD) [4, 5]. It introduces colour charges and their corresponding mediators, the gluons, which are explained in more detail in Sec. 2.2.2.

The combined $SU(2)_L \otimes U(1)_Y$ group symmetry corresponds to the electromagnetic and to the weak force [2]. They introduce the electrical charge Q and the weak isospin T , respectively. Those two forces further combine at very high energies via the electroweak unification [6]. The latter entails the unification of the electromagnetic force, originating from quantum electrodynamics (QED) [7–10], and the weak force, stemming from quantum flavour dynamics (QFD) [11–13]. The charge of the combined interaction is the weak hypercharge Y . However, the bosons $W^{0,1,2}$ and B^0 predicted by this symmetry are massless which is contradicting the massive bosons observed. This necessitates a process that introduces massive bosons.

The Brout-Englert-Higgs Mechanism [14–16] explains how bosons, and fermions as well, acquire their mass. The theory introduces a quantum Higgs-field. Every particle interact-

2 The Standard Model of Particle Physics

ing with the field becomes massive. At very high energies, this Higgs-field is symmetric. However, at energies which we observe under normal conditions, this symmetry is spontaneously broken [17, 18]. One of the results of this is a non-zero vacuum expectation value. This vacuum energy introduces additional terms to the Lagrangian, spoiling the electroweak symmetry. These additional terms mix the four massless bosons of the electroweak symmetry and introduce interactions between the $W^{1,2}$ and the Higgs-field [17]. This effect yields three massive bosons W^\pm, Z^0 and one massless photon γ . The W bosons are associated with the $SU(2)_L$ symmetry group. The remaining two bosons are associated with the $U(1)_Y$ symmetry group. All of these bosons are further discussed in Sec. 2.2.2.

Furthermore, one of the degrees of freedom introduced by the Higgs-field is not defined via the Brout-Englert-Higgs mechanism. It manifests as the scalar Higgs boson H [14]. The properties of this particle is also discussed more in Sec. 2.2.2.

2.2 Particles

The SM describes particles as elemental units of matter or forces. All particles have various properties such as mass, electrical charge and spin. Furthermore, each particle has an antiparticle that has the same properties as the complementary particle, but its electrical charge is inverted [19, 20]. These antiparticles are typically denoted with a bar on top of the particle identifier. Uncharged particles do not have a complementary antiparticle. At its core, the SM categorizes particles into two main groups by their spin. These groups are fermions and bosons which are explained in Sec. 2.2.1 and Sec. 2.2.2, respectively. In the following the focus will be on particles, since antiparticles have identical properties but with an inverted electrical charge.

2.2.1 Fermions

In the SM, fermions are one of the two fundamental classes of elementary particles, the other being bosons as described in Sec. 2.2.2. Fermions are particles with half-integer spin [20]. They are the basic constituents of matter and obey the Fermi-Dirac statistics as well as the Pauli exclusion principle [21]. Moreover, Fermions can be subdivided into quarks and leptons as further described in the following sections.

Quarks

Quarks are elementary particles that interact via the strong nuclear force, as well as the weak and electromagnetic forces which were introduced in Sec. 2.1. Quarks are classified

into three generations [20]. In each generation, there is an up-type and a down-type quark defined by their electrical charge and weak isospin [22]. The up-type quarks have a positive electrical charge of $+2/3$ times the elementary charge e and a weak isospin of $+1/2$. The down-type quarks have an electrical charge of $-1/3 e$ and a weak isospin of $-1/2$.

For each generation, a weak isospin doublet can be defined. To better describe these quarks, 6 flavours are defined [22]. Each quark flavour has unique properties. The first generation's doublet contains the up (u) and down (d') quark. The second generation consists of the charm (c) and strange (s') and the final and third generation includes the top (t) and bottom (b') quark.

Note that down-type quarks denoted as q' in the isospin doublets describe the weak eigenstate while q describes the mass eigenstate. These two eigenstates are related via the unitary Cabibbo-Kobayashi-Maskawa (CKM) matrix [22, 23]. The matrix describes the probability amplitude V_{ij} for the transition from quark flavour i to quark flavour j under the weak interaction. Furthermore, it describes the relation of the weak and mass eigenstates of down-type quarks

$$\begin{pmatrix} d' \\ s' \\ b' \end{pmatrix} = \begin{bmatrix} V_{ud} & V_{us} & V_{ub} \\ V_{cd} & V_{cs} & V_{cb} \\ V_{td} & V_{ts} & V_{tb} \end{bmatrix} \begin{pmatrix} d \\ s \\ b \end{pmatrix}. \quad (2.1)$$

The entries in the CKM matrix are not predicted by theory. Hence, the amplitudes must be measured experimentally. The current best fitted values [24] are the following:

$$\begin{bmatrix} V_{ud} & V_{us} & V_{ub} \\ V_{cd} & V_{cs} & V_{cb} \\ V_{td} & V_{ts} & V_{tb} \end{bmatrix} = \begin{bmatrix} 0.97373 \pm 0.00031 & 0.2243 \pm 0.2243 & 0.00382 \pm 0.00020 \\ 0.221 \pm 0.221 & 0.975 \pm 0.006 & 0.0408 \pm 0.0014 \\ 0.0086 \pm 0.0002 & 0.0415 \pm 0.0009 & 1.014 \pm 0.029 \end{bmatrix} \quad (2.2)$$

With increasing quark generation, the masses of the quarks also increases. The current best measurements of the masses for the up-type quarks and the down-type mass eigenstates [24] yield

$$\begin{aligned} m_u &= 2.16^{+0.49}_{-0.26} \text{ MeV}, & m_d &= 24.68^{+0.48}_{-0.17} \text{ MeV}, \\ m_c &= 1.27^{+0.02}_{-0.02} \text{ GeV}, & m_s &= 93.4^{+8.6}_{-3.4} \text{ MeV}, \\ m_t &= 172.69^{+0.30}_{-0.30} \text{ GeV}, & m_b &= 4.18^{+0.03}_{-0.02} \text{ GeV}. \end{aligned} \quad (2.3)$$

2 The Standard Model of Particle Physics

Quarks also carry a property known as colour charge [4, 5]. It is analogous to the electric charge but associated with the strong nuclear force. However, unlike electric charge, which comes in positive and negative values, colour has six possible states: red, green, blue and their complements anti-red, anti-green, and anti-blue. Quarks always combine to a state in which all three colours are combined, or any colour combined with its complement [5]. These states are called colourless. This is known as colour confinement and is responsible for the fact that isolated quarks are never observed in nature.

The Top Quark

The top quark will be explained in more detail since its of particular interest for this project. The discovery of the top quark took place in 1995 at FERMILAB through the efforts of the DØ [25] and CDF [26] experiments that both discovered the top quark independently. The top quark is acknowledged as the most massive among all quarks. Producing top quarks needs significant energies owing to high mass of the top quark. Such energies are attainable in hadron colliders. The top quark decays before it hadronises due to its brief lifetime is approximately $\tau_t \approx 5 \cdot 10^{-25}$ s [24]. It decays into a W boson and a down-type quark which then undergoes hadronisation.

The likelihood of decaying into a specific down-type quark is determined by the previously mentioned CKM matrix in Eq. 2.2. Comparing the values of V_{td} and V_{ts} to V_{tb} from Eq. 2.2 shows the predominant top decay mode to b quarks.

The W boson, the second particle from the top decay, also decays further. It can decay either into a charged lepton & neutrino pair or into a quark and antiquark pair. Thus, the resulting final state from a top decay include one quark and a lepton or three quark, depending on the W boson decay mode.

b tagging

To precisely identify t quarks, an accurate algorithm to distinguish b is necessary. The reason for this is the top quarks predominant decay mode into b quarks which was explained previously. To achieve this, b tagging is introduced [27, 28].

The accurate identification of works by exploiting the properties of the b quark. It has a relatively large mass and a long lifetime. The latter is explained by its suppressed decay modes. Equations 2.2 shows that the V_{tb} element is the highest values for b quark row. Thus, the b flavour couples predominantly to the t flavour and decay modes into other flavours are suppressed. However, the t is significantly heavier than the b quark as seen in Eq. 2.3. Hence, the decay into a top quark is also strongly suppressed.

Due to the long lifetime of the b quark, it can travel a measurable distance before decaying. Thus, its decay products do not originate from the primary vertex of the collision. Instead, reconstructing these decay products yields a displaced vertex position which is typically referred as ‘secondary vertex’. This reconstruction combined with the hard momentum spectra of the b quarks decay products yields a sufficiently accurate b tagging which reaches an efficiency of 70% [29] at the ATLAS experiment. This approach can also be applied, to a lesser extent, to charm tagging.

Leptons

Leptons are the second group of fermions. They do not experience the strong nuclear force and interact via the weak and electromagnetic forces. Analogue to the quarks, there are three generations of leptons: electron, muon and tau [20]. These are typically denoted as e , μ and τ , respectively.

Each generation consists of a weak isospin doublet containing an uncharged neutrino ν_l and its respective charged lepton l [20]. Charged leptons have an electrical charge of $-1e$ and a weak isospin of $-1/2$. Furthermore, the charged leptons are massive. Their masses increase with higher generations as current measurements [24] show

$$\begin{aligned} m_e &= 0.511 \pm 0.001 \text{ MeV}, \\ m_\mu &= 105.66 \pm 0.001 \text{ MeV}, \\ m_\tau &= 1776.86 \pm 0.12 \text{ MeV}. \end{aligned} \tag{2.4}$$

On the contrary, the uncharged neutrinos have no electrical charge [24], a weak isospin of $+1/2$ and are predicted to be massless by the SM [20]. However, the later prediction is conflicting with some observed phenomena that are explained in Sec. 2.3.

2.2.2 Bosons

Bosons are the second group of particles in the SM. Unlike the Fermions, bosons have integer values of spin and obey Bose-Einstein statistics [21]. Bosons can be subdivided into gauge bosons that mediate three of the four fundamental forces and the Higgs boson.

Gauge Bosons

In the SM there are 4 different gauge bosons types [20] that are responsible for the interaction between particles of the SM. While many of their properties differ, they all

2 The Standard Model of Particle Physics

have spin 1. The remaining properties are discussed in the following paragraphs.

The photon (γ) is the massless mediator of the electromagnetic force [7]. It itself is not electrical charged and thus, couples to positively and negatively charged particles equally. The behaviour of photons is determined by QED which was introduced in Sec. 2.1.

A gluon (g) is a type of massless gauge bosons that is responsible for the mediation of the strong nuclear force [4]. They couple to the colour charge of quarks. And unlike the photon, gluons themselves also carry colour charges which are exchanged during a strong interaction. There are eight different possible colour combination for gluons due to the rules of QCD. Since they carry the charge they couple to, gluons are able to couple to other gluons. These processes are called self-couplings.

Lastly, there are W^\pm and Z^0 bosons. These are the mediators of the weak nuclear force. In contrast to the other gauge bosons, these are massive due to symmetry breaking in the Brout-Englert-Higgs Mechanism which is explained in more detail in Sec. 2.1. Their masses were measured to be [24]

$$\begin{aligned} m_W &= 80.377 \pm 0.012 \text{ GeV}, \\ m_Z &= 91.1876 \pm 0.0021 \text{ GeV}. \end{aligned} \tag{2.5}$$

W^\pm bosons have an electrical charge of $\pm 1e$. Moreover, they have a weak isospin. Its third component of the weak isospin is ± 1 , respectively. Fermions interacting with the W bosons undergo a flavour transition. Charged leptons convert to lepton neutrinos and vice versa. Quarks also change their flavour. Their transition rate from one quark to the other is determined by the previously discussed CKM matrix. Couplings with the W bosons are CP violating. The Z^0 boson, as indicated by its superscript, has no electrical charge and its third component of the weak isospin is 0.

Higgs Boson

The Higgs boson (H^0) was the last particle of the SM discovered in 2012 [30, 31] by the combined efforts of the ATLAS [32] and CMS [33] experiments. The Higgs boson's detection gave strong support to the Brout-Englert-Higgs mechanism discussed in Sec. 2.1. It is electrically neutral and has spin 0, making it the only scalar boson. Moreover, it is the second-heaviest particle ever detected with current measurements [24] showing a mass of

$$m_H = 125.25 \pm 0.17 \text{ GeV}. \tag{2.6}$$

Furthermore, it represents the quantum manifestation of the Higgs field and thus, couples to mass of particles. Its production and decay branching ratios are strongly dependent on the mass of the interacting particle. The higher the mass, the stronger is the Higgs coupling resulting in higher branching ratios. The reason for this is the linearity between the Yukawa coupling strength and the (fermion) masses [20, 34]. Hence, the most common production modes are in combination with either t quarks or W/Z bosons.

For the decay, the most likely modes are decays into pairs of b quarks or W and Z bosons. While the Higgs coupling of the t is stronger than the b , the decay into a t quark pair is strongly suppressed, due to its significantly higher mass $2m_t > m_H$. Couplings with the Higgs field (thus also with the Higgs boson) are described as Yukawa couplings that also generate the mass of fermions and bosons [14, 16]. Since the Higgs boson is massive, it can couple to itself, similar to the gluon. This gives rise to Higgs self-coupling.

2.3 Beyond the Standard Model

Despite the incredible range of phenomena that the SM can predict and explain as well as its precision, certain phenomena contradict its fundamental explanations.

Neutrino Oscillation

One of these problematic observations is neutrino oscillation [35–37]. It describes how neutrinos change their flavour while propagating through space. The first indication was found by the Homestake Experiment in 1968. It detected solar neutrinos using a large tank of fluid and observed a neutrino deficit. In 1998, the Super-Kamiokande experiment studied atmospheric neutrinos and discovered a changing electron/muon neutrinos flux during the runtime.

The oscillation originates from the separation of the flavour eigenstates of the neutrinos (ν_e, ν_μ, ν_τ) and its mass eigenstates (ν_1, ν_2, ν_3). If these eigenstates are not equal, then neutrinos could change their flavour. The probability of a neutrino of a given flavour transitioning into another flavour depends on the mixing angles and mass differences between the mass eigenstates. The observed oscillation necessitates at least two massive neutrinos. Contradictory, the SM predicts all neutrinos as massless which would result in their flavour and mass eigenstates to be identical. Consequently, the oscillation would be prohibited and thus, the SM fails to account for neutrino oscillations.

Gravity

Another obvious problem with the SM is the absence of gravity. While the force of gravity is observed, the SM has no boson responsible for mediating gravity. Possible solutions include the introduction of a hypothetical massless and uncharged graviton [38] or string theory [39]. Without an explanation of gravity, the SM can not achieve to be a unified theory of everything.

Further Contradictions

There are more contradicting observations that need explanations beyond the SM. These examples contain, but are not limited to, dark matter [40–42], a type of invisible mass needed for stellar observations, prediction of vacuum energy [43], a deviation between QFT and cosmological predictions and the hierarchy problem [44], a relatively low Higgs boson mass that necessitates fine-tuning. For each of the problems, several BSM explanations such as supersymmetry [45] or modified gravity [46] are possible.

2.4 Higgs-Associated Top Quark Pair Production

TODO: IMPLEMENT ITS BACKGROUND CROSS SECTIONS SOMEWHERE

The targeted event topology is the Higgs-associated top quark pair production in which the Higgs boson decays into two W bosons. In the following, these events will be referred to as $t\bar{t}(H \rightarrow WW^*)$ events. The topology is a fully hadronic decaying $t\bar{t}$ pair with an additional Higgs boson being radiated. The latter decays to two W bosons which then further decay semi-leptonically, which means one W boson decays hadronically into two quarks while the other decays leptonically into a lepton neutrino pair.

Due to the insufficient mass of the Higgs boson to create on-shell W bosons [24], one of the two W bosons must be off-shell. This is denoted by the asterisk superscript W^* . To suppress backgrounds, the off-shell W^* boson is assumed to decay leptonically. Then the on-shell hadronic W boson can be directly reconstructed.

The corresponding Feynman diagram of the targeted topology can be seen in Fig. 2.1. The final state contains six quarks from the top quarks, two additional quarks from the hadronic W boson decay and one lepton & neutrino pair from the leptonically decaying W^* boson.

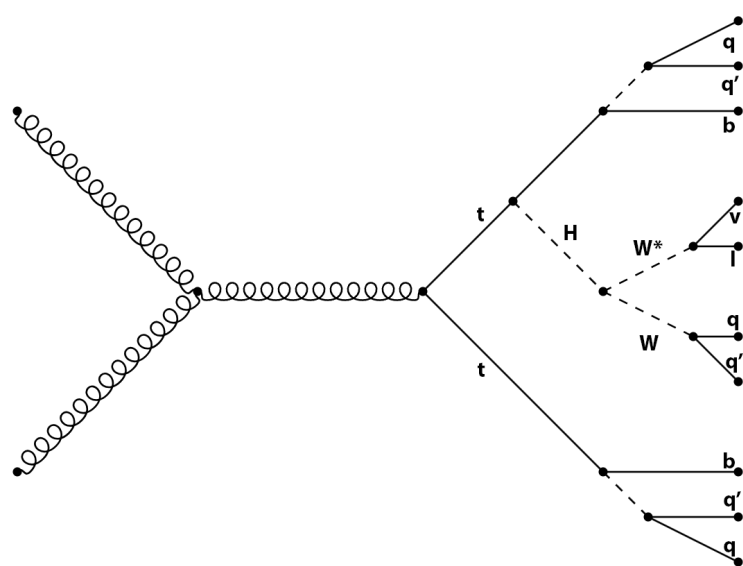


Figure 2.1: Feynman diagram of the targeted $t\bar{t}(H \rightarrow WW^*)$ event topology.

3 Experimental Setup

To collect data on $t\bar{t}(H \rightarrow WW^*)$ events, a high-energy particle collider is necessary. Additionally, a setup for signal detection and suitable reconstruction algorithms are required. This chapter introduces the Large Hadron Collider in Sec. 3.1 which is used for collecting the data for this project. It is one of the most important particle accelerators worldwide and includes many experiments such as the ATLAS experiment. The ATLAS experiment provides the data for the project and is discussed in great detail in Sec. 3.2. Other experiments are briefly described in Sec. 3.3.

3.1 Large Hadron Collider

The Large Hadron Collider (LHC) [47, 48] is the world's largest and most powerful particle accelerator. It's located underground near Geneva, Switzerland, straddling the border between Switzerland and France. Specifically, it's situated at the European Organization for Nuclear Research (CERN). The collider spans 27 km in circumference and reaches depths of up to 175 m. Along the collider, there are several detectors build which will be explored in Sec. 3.2 and Sec. 3.3. Fig. 3.1 shows and aerial view of the regions above the LHC demonstrating its size and showing the position of the different experiments.

It is used to create and accelerate bunches of protons close to the speed of light. Then a collision of these bunches is induced. During such a collision, partons from the protons interact and give rise to a large multitude of processes [19]. By studying the debris produced by these collisions, physicists can gain insights into fundamental questions about the nature of the universe. Moreover, predictions of the SM introduced in Ch. 2 can be tested with such collisions.

The LHC is operating for certain time periods with long shutdowns in between. The first operation period, Run I [49], which was active from November 2009 until February 2013. It started with a beam energy of 1.2 TeV which was then later increased to 3.5 TeV. In the last year it reached a beam energy of 4 TeV. During the operation, 5.6 fb^{-1} had been accumulated by ATLAS and CMS. Additionally, 1.2 fb^{-1} had been accumulated by LHCb. Then Long Shutdown 1 followed Run I.

3 Experimental Setup



Figure 3.1: Aerial view above the Large Hadron Collider showing its size. The different experiments are marked along the LHC course. ©CERN

In April 2015, Run II [50] started. The second run reached beam energies of 6.5 TeV and lasted until December 2018. It acquired an integrated production of 160 fb^{-1} . The Long Shutdown 2 then held on until 2022.

The currently active Run III [51] launched in April 2022 with a centre-of-mass energy of 13.6 TeV, 6.8 TeV per beam. It is planned to operate until the coming Long Shutdown 3 planned for 2026.

3.2 The Atlas Experiment

ATLAS (A Toroidal LHC ApparatuS) [52] is one of the four main experiments at the LHC. Its detector is designed as a general-purpose detector to explore a wide range of physics phenomena [53, 54]. The detector began its operation along the start-up of the LHC. It spans a height of 25 m and a length of 44 m. It is build almost hermetically around the LHC beam pipe as a toroidal shape which can be seen in Fig. 3.2. Constructing the detector so close to the interaction point allows measuring the maximum possible phase space. Within the detector, there are several layers that are explained in great detail in Sec. 3.2.1. The coordinate system used in ATLAS is important for this project and is explained in Sec. 3.2.2.

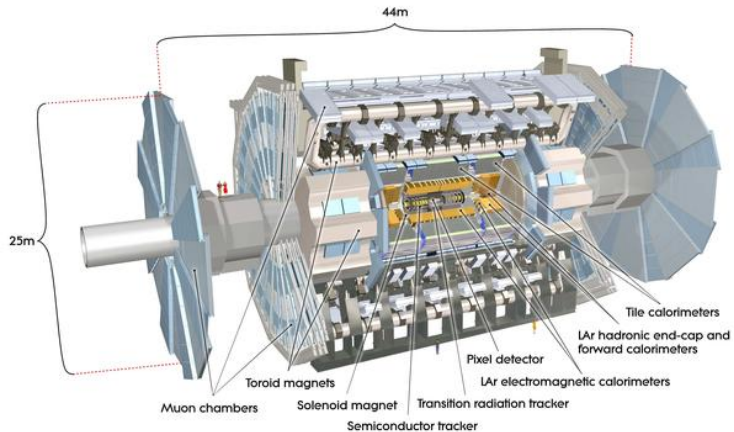


Figure 3.2: Overview of the ATLAS detector showing its size and structure. Moreover, every important component is labelled. ©BMBF

3.2.1 Detector

The detector of the ATLAS experiment is of particular interest. The following sections will cover its elements including the detector modules and magnetic systems in great detail. An overview of the detector is shown in Fig. 3.2. The individual layers of the detector are further visualised in Fig. 3.3.

Magnetic System

For the measurement of particle trajectories and their curvature, significant magnetic fields are required. For that reason, ATLAS implemented superconducting magnet system build from Aluminium, Copper and Niobium-Titanium. alloy.

It includes a central solenoid magnet surrounding the Inner Detector. It provides a central field of 2 T [53]. Since the central solenoid is placed right before the calorimeter, this magnet is build as thin as possible.

Furthermore, three large air-core toroids generate an additional magnetic field for the outer muon spectrometer. Each consisting of eight symmetrical coils placed radially around the beam axis [53]. These magnet systems are cooled using liquid Helium at 4.5 K [53].

The Inner Detector

The Inner Detector [55, 56] is a combined system of high-resolution detectors close to the beam pipe and continuous tracking elements at outer radii. Its task is to measure the particles' momentum. As mentioned before, the complete Inner Detector is surrounded by the 2 T central solenoid magnet. Charged particles are deflected inside the detector, due

3 Experimental Setup

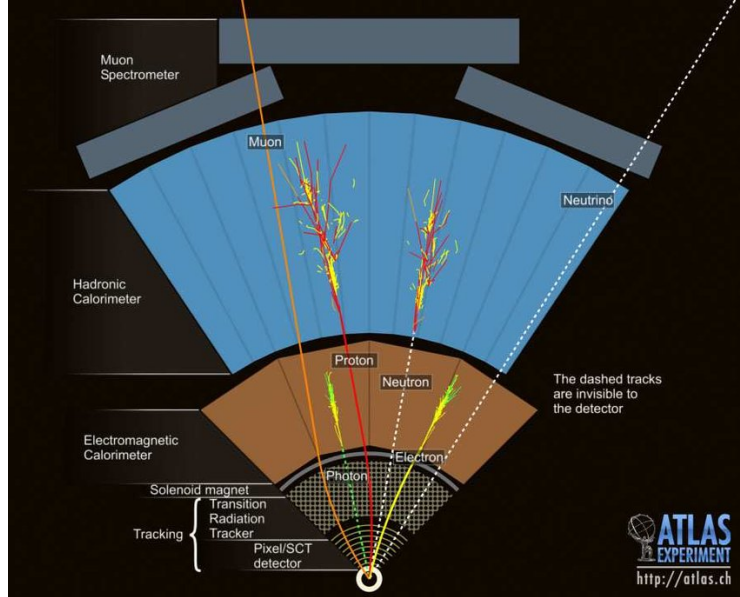


Figure 3.3: Cross-section of the concentric layers within the ATLAS detector. ©CERN

to the Lorentz force [19]. By precisely measuring the curvature, momentum measurements and particle track reconstruction are achieved.

All modules are placed either in the barrel or the end-cap region. The first region is arranged on concentric cylinders surrounding the beam axis and typically covers the low η region. The later region's detectors are installed on disks perpendicular to the beam axis and cover the remaining space for a full coverage up to $\eta \pm 2.5$.

The innermost detector tiles are semiconductor pixel detectors [53, 57]. The first barrel layer is only 4 cm from the beam pipe, covers an area of 0.2 m^2 and measures the complete space up to $\eta = \pm 2.5$. It reaches a resolution of $\sigma_{R\phi} = 12 \mu\text{m}$ and $\sigma_z = 66 \mu\text{m}$. This layer is followed by two more barrel layers that cover $\eta = \pm 1.7$ and reach the same resolution. To compensate this lower η acceptance, 5 end-cap disks are placed in each side. These cover the remaining space up to $\eta = \pm 2.5$. Each module is only 21.4 mm wide and 62.4 mm long containing 61440 pixels controlled 16 chips. Every pixel detector has its individual circuit including buffering to store data until the trigger decision. While the precision and radiation resistance of these pixel detectors are remarkable, they also introduce some material before the calorimeters and are expensive. Hence, the amount of pixel detectors that can be included in the detector is limited.

Directly surrounding the pixel modules, the silicon strips are introduced [53, 58]. It is subdivided into four barrel layers for the η range up to $\eta = \pm 1.4$ and 9 end-cap wheels on each side for the remaining space up to $\eta = \pm 2.5$. They achieve slightly lower precision compared to the pixel modules with resolution achieving $\sigma_{R\phi} = 16 \mu\text{m}$ and $\sigma_{z/R} = 580 \mu\text{m}$.

Each detector is $6.28 \times 6.40 \text{ cm}^2$ in size and includes 768 strips. Moreover, each module consists of four of these silicon detectors.

Straw tube trackers around the previous modules allow for a lot of measured tracking points [53, 59]. In the barrel regions, these are placed parallel to the beam axis. In contrast to the end-caps where these are aligned perpendicular to the beam axis. Previously, these were filled with a Xenon gas mixture. However, due some leakage this Xenon was changed to Argon to reduce costs. While these achieve significantly worse resolutions of $\sigma = 170 \mu\text{m}$, they can cover a greater area to their lower cost and less material per tracking point. Hence, they strongly contribute the precise momentum measurements.

The Calorimeters

The calorimeters [53, 60] are used to detect charged particles by absorbing them, allowing for a measurement of their deposited energy. The physical process of showering which allow such measurements was previously described in Ch. 2. ATLAS' calorimeter system is subdivided into four parts: electromagnetic calorimeter, hadronic barrel calorimeter, hadronic end-cap calorimeter and hadronic forward calorimeter.

The first of these calorimeters, the electromagnetic calorimeter [53], is built from Lead, liquid Argon and Kapton electrodes. It covers the pseudorapidity range up to $\eta = \pm 3.2$ while the barrel region can detect up to $\eta = \pm 1.475$. It is the innermost calorimeter and is primarily responsible for detecting photons and electrons.

The hadronic calorimeter [53] is build around the electromagnetic calorimeter and is build from plastic scintillator plates and Iron absorber in the barrel region and from Copper, Lead and liquid Argon in the end-cap regions. This separation is done to optimise the detector for the varying requirements of the great η range. The barrel region reaches up to $\eta = \pm 1.7$ and the end-caps up to $\eta = \pm 3.2$. Its thickness is one of the most important parameters for the calorimeter, since it has to be sufficiently thick to contain the hadronic showers and thus, minimize punch-trough into the adjacent Muon Spectrometer.

The forward hadronic calorimeter [53] is implemented to cover the strongly boosted region of $3.1 < |\eta| = 4.9$. It as well is build from a Lead liquid Argon mixture with additional electrodes from Copper or a Tungsten alloy.

The Muon Spectrometer

The outermost measurement part of the ATLAS detector is the Muon Spectrometer [53, 61]. It bends the muon tracks by utilising the previously explained air-core magnets. The magnetic field is mostly orthogonal to the muon trajectories. In the region up to $\eta = \pm 1.0$ the large barrel toroid magnet provides the needed magnetic field. Within the acceptance

3 Experimental Setup

range of $1.4 \leq |\eta| \leq 2.7$ two smaller end-cap magnets bend the tracks. Between of these regions is the transition region where the deflection of the muon trajectories is done by the magnet field of both magnetic systems. The muon spectrometer consists of four parts.

The first part is the monitored drift tube chamber which make up 800 m^3 in volume. It consists of 30 mm diameter aluminium tubes operating with a mixture of 93% Argon and 7% CO₂. The single-wire resolution is $\sim 80\text{ }\mu\text{m}$. To increase the overall resolution, multilayer pairs of multiple tubes are utilised.

The New Small Wheel project replaced the original Cathode Strip Chambers [61–63]. It was installed after Run II and uses Micro-Mesh Gaseous Structure as well as small-strip thing gab chambers. The former being a detector consisting of a planar electrode and a thin steel mesh forming a drift chamber. It is filled with the same Argon-CO₂ mixture as the first drift tube chamber. Its spatial resolution reaches $73\text{ }\mu\text{m}$. The later thing gab chambers consist of a Gold-plated Tungsten wire grid placed between two electrodes. The electrodes are made from a Carbon-epoxy mixture. The detector module reaches a spatial resolution of $100\text{ }\mu\text{m}$ at the rate of up to 20 kHz/cm^2 .

The resistive plate chambers [53, 61, 62] are another gaseous detector. It uses a non-flammable C₂H₂F₄ SF₆ gas mixture. Again, the electrodes of the detection chamber are made from Carbon. The panels themselves are made polystyrene placed between Aluminium sheets. They achieve a spatial resolution of 1 cm and a temporal resolution of 1 ns.

The thin gab chambers [53, 61] are the last chamber of the muon spectrometer. It is a proportional chamber using a flammable gas mixture of 55% CO₂ and 45% n-pentane. Even though it needs additional safety precautions, it is less sensitive to mechanical deformations, yields nearly Gaussian pulse height distributions and has a small dependence on the incident angle. The distance of both electrodes are 2.8 mm.

Trigger System

The aforementioned detector systems are able to detect and record significant amounts of data. The initial interaction rate of $\sim 1\text{ GHz}$ resulting in a bunch-crossing rate of up to 40 MHz [53] are too much to save. Approximately only 0.1 kHz of data is suited for permanent storage. Thus, a very fast selection must be defined and implemented that discards most of the events to a manageable level. For that purpose, an online multi-level trigger system is introduced. Each trigger level refines the selection done from the previous level.

The first level (LVL1) trigger [53, 64] makes the initial selection. It utilises several subsets of detectors with reduced resolution to quickly decide whether the recorded event

is saved or discarded. This is done by identifying potential candidates. The LVL1 decision is then based on certain object requirements. The maximum rate for the LVL1 trigger is up to 75 kHz, targeting a decision latency of up to $2\ \mu\text{s}$. The selected events of the LVL1 trigger are temporary saved into readout drivers and then readout buffers.

The event data stays on the readout buffers until the LVL2 trigger [53, 65] either rejects or accepts them. The second trigger level utilises the region-of-interest information provided by the LVL1 trigger. It includes information on the position and momentum of potential objects and the sums of transverse energies E_T and E_T^{miss} . The LVL2 trigger uses only the necessary information but has access to the full resolution information from the detectors. The LVL2 trigger reduces the rate to around 1 kHz. Its latency is variable but in the range of 1-10 ms. Events that pass both triggers are then transferred to an offline event filter system that performs the final selection. The final output data rate is approximately 100 MB/s.

3.2.2 Coordinate System

The ATLAS detector is built as a cylinder. Thus, a fitting coordinate system must be defined. For that, every position in the detector is defined by the z position parallel to the beam axis, the azimuth angle ϕ along the detector and the pseudo-rapidity η with respect to the collision point of the detector. Figure 3.4 shows qualitatively how the detector coordinate looks like when the detector cylinder is rolled out and projected onto a 2 dimensional plane.

To properly work with spatial separations in this coordinate system, the variable

$$\Delta R = \sqrt{(\Delta\phi)^2 + (\Delta\eta)^2} \quad (3.1)$$

is introduced. It represents a cone around each point in the coordinate system as shown in Fig. 3.4. This should not be confused with R which is typically the radius from the beam pipe. Hence, expressions such as $R\phi$ correspond to the radial scaled azimuth angle and is used in classifying detector resolutions as seen before.

3.3 Other Experiments

Besides the discussed ATLAS experiment, there are three more main experiments at the LHC: CMS, ALICE and LHCb. This section will briefly mention each of these experiments and compare them to the ATLAS experiment.

3 Experimental Setup

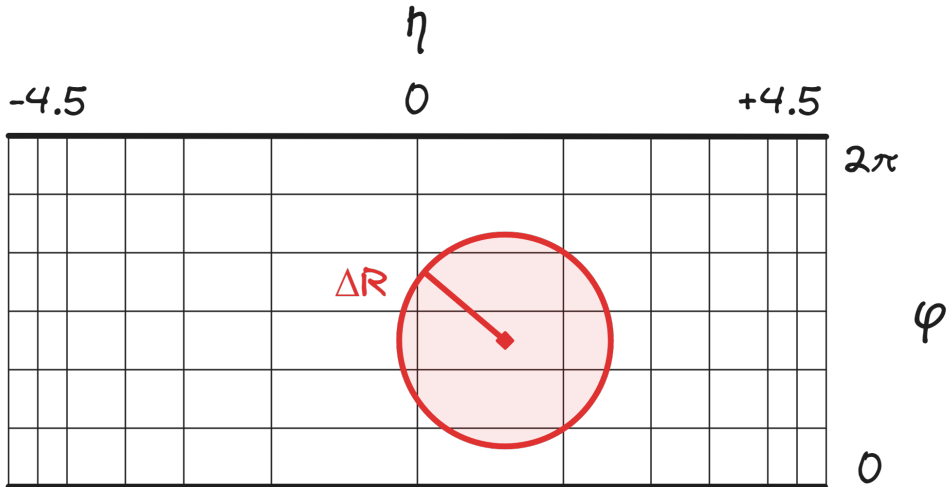


Figure 3.4: Sketch visualising the ATLAS coordinate system using the azimuth angle ϕ and pseudo-rapidity η . It represents the rolled out detector cylinder. Moreover, it shows how a spatial cone defined by ΔR would look like.

The CMS (Compact Muon Solenoid) [66] detector is a general-purpose similar to the ATLAS detector. Its detector is shown in Fig. 3.5. As its name suggest, a particular focus is set on the precise measurement of high energy muons over a wide range of angles and momenta. Its main goals include muon mass resolution of around 1% at 100 GeV and the ability to determine the charge of muons with momentum $p < 1$ TeV. Other main goals include the reconstruction of charged particles, efficient tagging of τ leptons and b quarks, precise missing transverse energies and isolation of photons and leptons at high luminosities. CMS started its operation with the commissioning of the LHC.

The ALICE (A Large Ion Collider Experiment) [67] focuses on heavy ion collisions. It is designed to measure the physics of strongly interacting matter and the quark-gluon plasma at extreme energies and temperatures. It consists of a central barrel which covers polar angles from 45° to 135° and a forward muon spectrometer covering 2° to 9° . The detector layout is further visualised in Fig. 3.6. While the ALICE physics program includes the study of light atoms, the main study utilises heavy nuclei Lead-Lead collisions. Its first collisions was recorded in November 2010.

LHC_b (Large Hadron Collider beauty) [68] is dedicated to study particles that contain b quarks, which sometimes are referred as beauty quarks. Unlike the other experiments, its detector is build as a single-arm spectrometer which can be seen in Fig. 3.7. It covers a forward angle of approximately 0.5° to 17° . The reason lies in LHC_b's focus on detecting b hadrons which are predominantly produced in forward and backward cones. The LHC_b experiment started the operation at the same time as ATLAS and CMS.

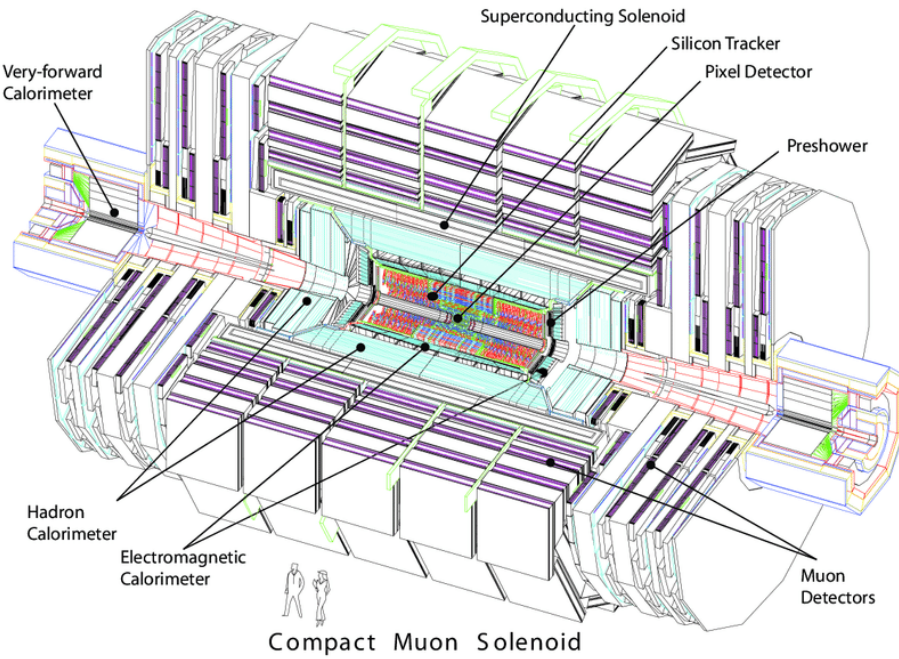


Figure 3.5: Overview of the CMS detector ©CERN

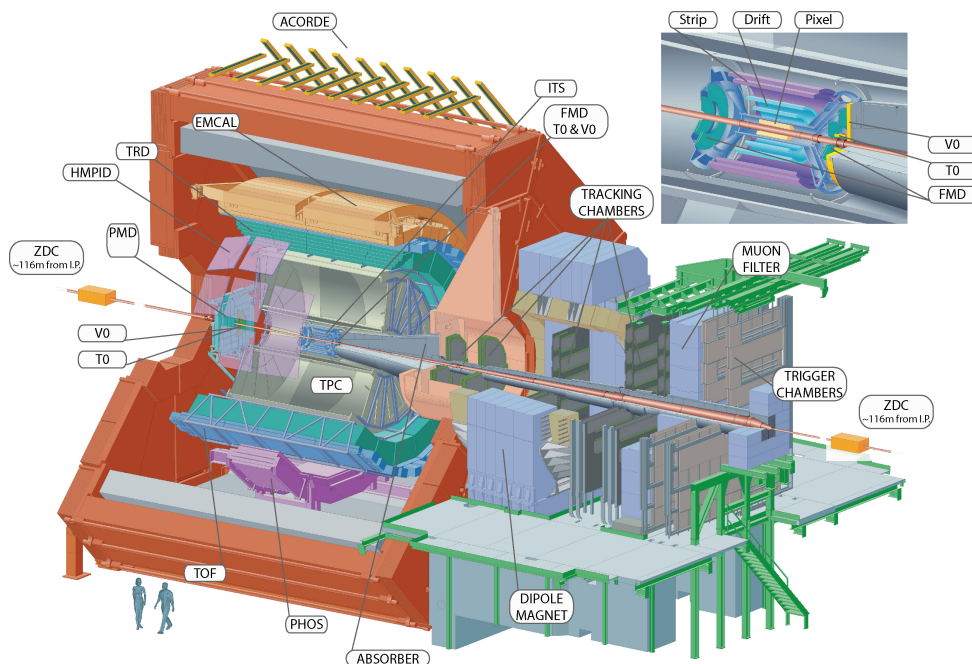


Figure 3.6: Overview of the ALICE detector ©CERN

3 Experimental Setup

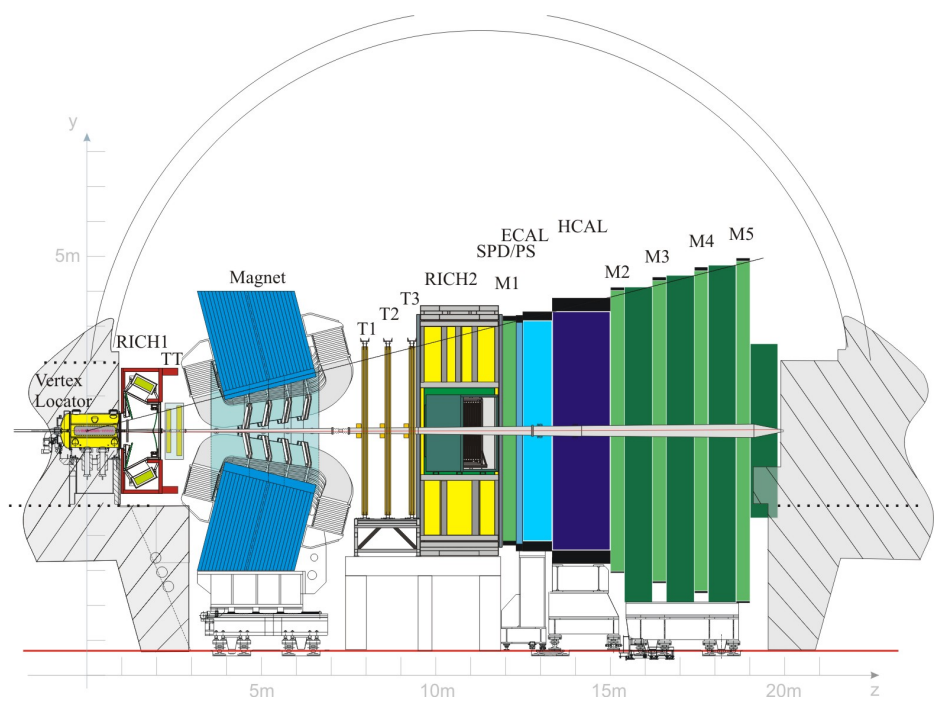


Figure 3.7: Overview of the LHCb detector ©CERN

4 Methods

TODO RENAME CHAPTER TODO HOW ARE TTHWW EVENTS SELECTED =>
ASK BAPTISE ABOUT THAT TODO WHY ARE WE EVEN INTERESSTED IN
THAT S? TODO EXPLAIN CLASSICAL ALGORITHMS IN MORE DETIAL - KINDE-
MATIC LIKELIHOOD FITTER (DEVELOPED BY GÖTTINGEN GROUP; JADA-
JADAJADA) TODO EXPLAIN WHY WE ASSUME ONSHELL HADRONIC DECAY
=> EASIER BACKGROUND SUPPRESSION

The goal of this project is to fully reconstruct the $t\bar{t}(H \rightarrow WW^*)$ events which were introduced in Sec. 2.4. Only the fully hadronic $t\bar{t}$ and semi-leptonic $H \rightarrow WW^*$ decay mode is targeted. Classical combinatoric algorithms are not suited for this task, since the final state has 8 jets. Furthermore, the final state contains an undetected neutrino which needs to be reconstructed. Thus, a modern approach using neural networks and sampling is implemented.

Section 4.1 covers the implementation and training of **SPA-Net**, a modern transformer for jet reconstruction. Its task is to match the jets of the fully hadronic $t\bar{t}$ system. After the $t\bar{t}$ system is matched, the remaining jets can be used to reconstruct the $H \rightarrow WW^*$ decay.

On-shell Higgs bosons can not decay into two on-shell W bosons. Hence, one of the W bosons is expected to be off-shell. We assume that the on-shell W boson decays hadronically. Then two of the remaining jets with an invariant mass closest to the W boson SM mass are matched to the on-shell W boson. The remaining off-shell W boson is then assumed to decay leptonically. The missing parameters due to the unknown off-shell W^* boson mass and the undetected neutrino ν_l are sampled using neutrino weighting as described in Sec. 4.3.

4.1 SPA-Net

TODO EXPLAIN MASHINE LEARNING AND DNNS => OWN CHAPAER? TODO
CHECK IF SPANET IS PRETRAINED OR NOT TODO HOW AND WHY IT UTI-
LIZES EVENT symmetries TODO EXPLAIN THE DIFFERENT VERSIONS OF SYYME-

4 Methods

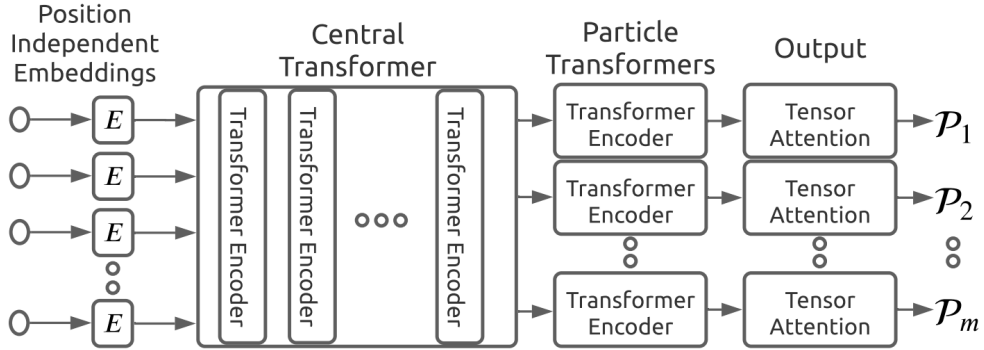


Figure 4.1: Overview of SPA-Net’s architecture and its four regions [69].

TRIES SUED IN SPANET MORE CLEARLY TODO LOOK AT UPDATED SPANET VERSION WITH NEW IMAGE TO INCLUDE AND LEPTON/MET INPUTS TODO EXPLAIN SYMMETRIC TENSOR Attention TODO COMBINED SYMMETRIC LOSS ONLY DURING TRAINING; DURING INFERENCE SPANET ITERATIVELY ASSIGNS JETS TO RECONSTRUCTED PARTICLES BY COMPARING THE SCORES OF INDIVIDUAL PERMUTATIONS SO THAT NO JET IS ASSIGNED TO MULTIPLE PARTICLES

For this project, the pretrained transformer network **SPA-Net** (Symmetry Preserving Attention Networks) [69] is used. It is able to match jets to predefined objects which we expect in the final state. It utilises symmetries in the event topology. These symmetries typically describe particles and anti-particles which are identical disregarding their charge. Moreover, when particles such as the W boson decay, they produce two particles. Since physics is invariant under swapping the labels of these two particles, they also define a symmetry that is used.

The architecture of this neural network is visualised in Fig. 4.1. It can be subdivided in to four components [69]: jet input embeddings, central transformer, particle transformers and self-attention output layer.

Each prediction is split into three steps. First, the amount of valid jet assignment permutations is reduced by splitting up event into sub-structures which are predefined by the event topology. Then each sub-structure is solved by assigning the best fitting jet to parton by applying a modern ‘Symmetric Tensor Attention’ [69]. All solved sub-structures are then combined into a final jet-to-parton prediction by using a combined symmetric loss [69]. Splitting up the individual particles allows partial event reconstruction. Furthermore, partial events can be used in training while still provide impactful signal.

In comparison to other neural networks, SPA-Net offers three main advantages: [69]

- The network is agnostic to the number of input objects (jet multiplicity). Hence, training and prediction can be done with samples that contain events with different number of jets.
- All predicted jet matches are unique. No object is matched to more than one jet. Furthermore, each prediction is also rated using an assignment probability that represents SPA-Net’s confidence for that particular prediction.
- Expected symmetries due to the event topology can be predefined. These symmetries are then preserved and used to speed up the process by simplifying the prediction task.

Since the neural network is pretrained on $t\bar{t}$ events, some fine-tuning is needed for the $t\bar{t}(H \rightarrow WW^*)$ events. However, since this event channel has not been analysed before, no training samples are pre-made. Sec. 4.2 explains how the $t\bar{t}(H \rightarrow WW^*)$ training set for fine-tuning is created.

4.2 Truth Matching

To train SPA-Net, some training samples must be prepared as described in Sec. 4.1. Hence, a truth matching algorithm needs to be developed. It must take the truth and reconstructed information of well-defined MC simulations as inputs and outputs a corresponding jet for each expected final state particle.

For matching a jet to a truth particle, a spatial ΔR cone is placed around each jet. The cone size is limited to $\Delta R \leq 0.4$. Any truth object within a jet cone is saved as a potential match to the corresponding jet. However, if multiple particles are within one cone this would lead to non-unique assignments.

Hence, a final selection must be made if more than one truth object is potentially matched to a jet. After selecting one of the jets as the final candidate, this jet is then saved and made unavailable for other objects. Repeating this process yields samples that can be used as SPA-Net training input. Results from this truth matching algorithm are discussed in Ch. 5.

4.3 Neutrino Weighting

TODO FIND ORIGINAL NEUTRINO WEIGHTING PAPER => LOOK FOR REFERENCES IN THAT PAPER; PROBABLY DZERO DID IT TODO CURRENT CITA-

4 Methods

TION USAGE AS REFERENCE ON HOW TO USE NEUTRINO WEIGHTING FOR BACKGROUND SUPPRESSION OF

Neutrino Weighting [70] is used for the reconstruction of the leptonically decaying W^* boson in the $H \rightarrow WW^*$ subprocess. The problem of the unconstrained and unknown parameters due to the off-shell mass of the W^* boson and the neutrino are solved by introducing some assumptions.

First, we assume that the Higgs boson has a fixed mass of $M_H = 125.09\text{ GeV}$ [24]. Additionally, the mass of the on-shell W boson is assumed to be $M_W = 80.379\text{ GeV}$ [24]. Then, to fully reconstruct the $H \rightarrow WW^*$ sub-structure, we sample several combinations of the off-shell mass M_{W^*} and the pseudo-rapidity of the neutrino η_ν .

Using these assumptions, the $H \rightarrow WW^*$ subsystem is fully constrained [70] and the neutrino transverse momentum p_T^ν can be calculated. To compare the calculated neutrino momentum to the observed missing momentum, the weight

$$w = \exp \frac{(p_x^\nu - p_x^{\text{miss}})^2}{\sigma_x^2} \cdot \exp \frac{(p_y^\nu - p_y^{\text{miss}})^2}{\sigma_y^2} \quad (4.1)$$

can be calculated. The variable $\sigma_{x/y}$ is the experimental resolution of the missing momentum $p_{x,y}^{\text{miss}}$. The weight w is in the range of $[0, 1]$. Higher values mean better agreement between the calculated values and the observation. If the weight is calculated for many samples of M_{W^*} and η_ν , a plot as seen in Fig. 4.2 can be created. It shows the most likely combination of the unknown parameters.

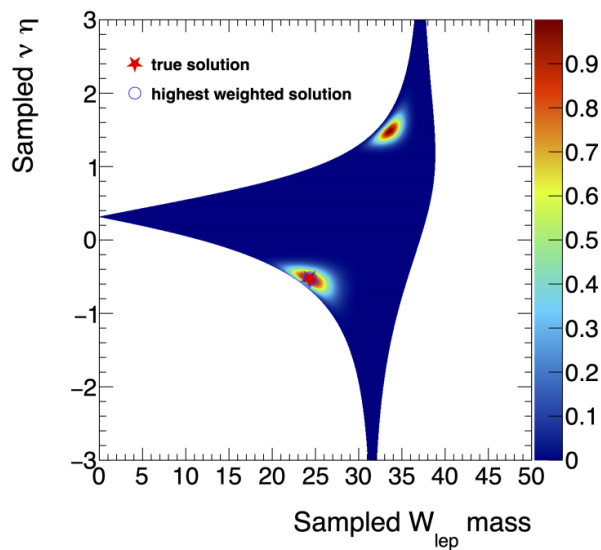


Figure 4.2: Example plot showing a potential distribution of weights for several sampled combinations of η_ν and M_{W^*} . The most likely combination of parameters can be seen at the red peaks [70].

5 Current Status

The project started on the 3rd of November 2023 and has been going for 5 months so far. During that time, the needed truth matching algorithm has been developed, validated and refined. Additionally, an environment for training **SPA-Net** on the ‘National Analysis Facility’ (NAF) from DESY was implemented. Section 5.1 explains the work done for the truth matching algorithm.

5.1 Truth Matching

The following paragraphs will outline the algorithm for preparing **SPA-Net** inputs. The fundamental idea of the matching is discussed in Sec. 5.1.1. Results of the validation are given in Sec. 5.1.2, 5.1.3 and 5.1.4 which cover the success rate, final jet selection scheme and Higgs decay regions, respectively.

5.1.1 Truth Matching Algorithm

As mentioned in Sec. 4.1, the need for training input motivates the development of a matching algorithm. A simple selection was developed that takes the MC simulations and begins by sorting the RECO- and TRUTH-trees and pairing the event information from both trees.

Then, for every expected particle from the event topology a match to some reconstructed jet is attempted. For such match, a spatial cone around every truth particle is considered. The cone is defined by $\Delta R \leq 0.4$ as introduced in Sec. 3.2.2. Every jet within the ΔR cone is then saved as a potential match.

If no jet is found within the cone, then the particle can not be matched. If exactly one jet is found, the potential match is saved as the final matched jet to the particle. For cases with more than one potential match, an additional step has to be implemented to decide which of the potential matches is selected. This is explained in more detail in Sec. 5.1.3.

The algorithm tries to first match a jet to each of the six final state particles from the fully hadronic $t\bar{t}$ system. Then, the algorithms attempts to reconstruct both W bosons. For successfully reconstructing the W boson, both decay quarks must be matched. Their

5 Current Status

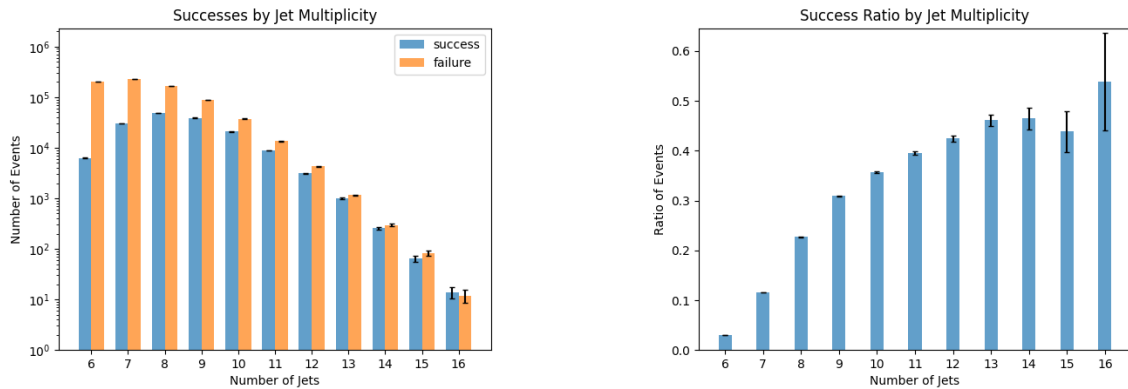


Figure 5.1: Overview of the total successful event count (left) and relative success rate (right) for the matching algorithm subdivided by the number of jets in the event.

four-vectors are added to recreate the W boson's four-vector. The t quarks can then be reconstructed if their corresponding b and W boson is matched. Again their four-vectors are added for the top quark four-vector.

An event is defined as a successful match, if both top quarks - and thus all decay particles of the fully hadronic $t\bar{t}$ system - are matched. The $H \rightarrow WW^*$ subsystem is not matched by this algorithm yet. Soon, the hadronic W boson decay will also be added into the matching algorithm. Then, **SPA-Net** will be trained on all jets of the events and its prediction can be directly used in neutrino weighting.

5.1.2 Successful Event Matches

The first results can be seen in Fig. 5.1 which features two summarising plots that show the success rate of the matching algorithm per jet multiplicity. Only the success of a total event match is shown.

More jets in the final state are expected to increase the chance for successful event matches since more jets are available. This expectation is fulfilled. However, the statistics decreases for higher jet multiplicities, because every additional jet originating from some parton needs to come from some higher-order physics process with additional couplings. Events with less than 6 jets can not fully match the expected $t\bar{t}$ system. Hence, these are not investigated.

For the training, all events with at least 6 jets will be used to maximize the available training statistics. Even events that are classified as failures for full event matches are expected to increase the training performance. This is justified by the fact that failed event matches can still contain successful particle matches that can be trained on.

Table 5.1: Overview of the three different matching schemes tested for the final jet matching. It shows the success fraction for each object and the combined $t\bar{t}$ system. The highlighted ΔR only approach yields the best results.

	successful matching in %				
	$t\bar{t}$	t	\bar{t}	W_t	\bar{W}_t
ΔR only	17.6	43.9	44.1	53.4	53.6
ΔR and Δp_T	17.5	43.7	43.9	53.1	53.2
Δp_T only	17.4	43.6	43.9	53.0	53.2

5.1.3 Final Jet Selection

To optimise the matching in the case of multiple possible matches, three different matching schemes were tested. The first scheme compares the spatial separation between the potential jets and the targeted particle. The closest jet in ΔR is then selected as the final match. The second approach focuses on the Δp_T of the potential jets and the targeted particle. The closest pair in momentum space is then selected. This scheme is motivated by the CP violating properties of the W boson which should result in non-symmetric transverse momenta for the decay particles. One last scheme was tested which combined the information of the ΔR and Δp_T approach. For the combined scheme, the ΔR was scaled to a range of [0,4] and Δp_t to a range of approximately [0,~10]. The latter one is not exact since it has no cut applied. Then, the pair that minimises both variables is chosen as the final match.

The result of the matching success fractions per particle are summarised in Tab. 5.1. The ΔR scheme performs the best and is used in future investigations. Interestingly, the different schemes change the results only by small amounts <1 %. Investigations showed that less than 20 % of events have any truth object with more than one potential match. Furthermore, these cases often choose the same final match regardless of the applied matching scheme. Hence, no further investigation into the final matching procedure was performed.

5.1.4 Higgs Decay Modes

Finally, an overview of different regions defined by the jet multiplicity and H/W decay modes can be seen in Tab. 5.2. It shows the relative yield for each region (using a total 4M event dataset) and the ratio of successfully matched events.

Immediately, the difference between the ≥ 5 and ≥ 6 jets region becomes clear. While the first region with any H decay and at least 5 jets in final state includes all events, the second region has a higher match success rate of 17.6 % instead of 15.8 % for full $t\bar{t}$

5 Current Status

Table 5.2: Overview of several regions defined by jet multiplicity and decay modes showing their relative yield to the total data set and matching success rates. The last three regions are events with $H \rightarrow WW^*$ decays, subdivided into fully leptonic, semileptonic and fully hadronic WW^* decays. The highlighted row corresponds to the targeted topology.

	rel. yield	successful matches in %				
		$t\bar{t}$	t	\bar{t}	W_t	\bar{W}_t
(all) ⁵⁺ jets	100.0%	15.8	41.0	41.2	50.5	50.7
(all) ⁶⁺ jets	90.1%	17.6	43.9	44.1	53.4	53.6
$(H \rightarrow bb)^{6+}$ jets	58.3%	16.5	42.6	42.8	53.5	53.6
$(H \rightarrow WW^*)^{6+}$ jets	1.2%	21.0	47.7	48.0	54.8	54.9
$(H \rightarrow WW^*)^{6+}$ jets fully leptonic	1.0%	21.2	48.2	49.3	55.2	55.2
$(H \rightarrow WW^*)^{6+}$ jets semileptonic	0.2%	19.9	45.5	46.6	52.6	53.7
$(H \rightarrow WW^*)^{6+}$ jets fully hadronic	0.0%	-	-	-	-	-

matching. This is expected as seen in Sec. ???. Furthermore, we can select certain H decay modes such as $H \rightarrow bb$ or more importantly $H \rightarrow WW^*$.

The targeted topology is highlighted in the table and shows that around 0.2% of all events are in this region. This is lower than expected. The cause for this lies in the identification from the events using the decay `PDGIDs`. Around 90 % of all events including a $H \rightarrow WW^*$ substructure have ill-defined `pdgIds`. Hence, these events are not classified and discarded resulting in lower statistics. A new sample with fixed truth records is expected to be available later in the analysis. If the statistics for training `SPA-Net` becomes a problem in the future, this will be investigated further. For now, the events are used for training as it is.

Note that the last row (fully hadronic $H \rightarrow WW^*$) behaves differently than one might expect initially. The branching ratio of W bosons would favour hadronic decays, yet no full hadronic decays are seen in the MC Simulations. This behaviour is also expected to be caused by the broken `pdgIds`. However, it is important to keep in mind that even with a fixed sample, the implemented single-lepton trigger will reduce the observed branching ratios. This reduction is due to the fact that events with no high p_T lepton are discarded and the $t\bar{t}$ system is targeted to decay fully hadronically. Hence, the other high p_T leptons can only originate from effects such as radiation or NLO processes.

5.2 NAF Computing Grid

Furthermore, after obtaining a certificate from the ‘Deutsche Forschungsnetz’ (DFN) and gaining access to the NAF cluster, `SPA-Net` was installed alongside training datasets of

5.2 NAF Computing Grid

different sizes. Some complications due to disk space and incompatible driver versions slowed down the implementation. The first dummy training ran successfully. Now the workflow for training and fine-tuning SPA-Net has been established.

6 Outlook

The following sections provide a brief overview of the planned steps of this project.

Fine-Tuning and Training SPA-Net

Now that **SPA-Net** is installed and ready to use on the NAF computing cluster as described in Ch. 5, it can be fine-tuned. Using a smaller training set, several versions of **SPA-Net** will be trained independently. These versions differ by their choice of hyperparameters and will be compared to find the best performing network. The optimised version of **SPA-Net** will be used as the final model. After the hyperparameter optimisation, **SPA-Net** will be trained on a greater dataset. Then, the fully hadronic $t\bar{t}$ system will be reconstructable.

Implementing Neutrino Weighting

TODO: REWRITE - EXPANDING SPANET TO RECONSTRUCT HADRNOC W FROM H; THEN INPUT 4VECTOR JET + LEPTON + MET TO GET MOST LIKEY MASS AND ETA WITH A LIKELIHOOD!

To reconstruct the other subsystem of the $t\bar{t}(H \rightarrow WW^*)$ system, neutrino weighting as explained in Sec. 4.3 will be implemented. The final algorithm is expected to take the event information and **SPA-Net**'s prediction as inputs. Its output should contain two of the remaining jets for the hadronic W boson decay as well as the prediction about the leptonic W^* boson decay. More specific, the most likely combination of off-shell mass M_{M^*} and eta of the neutrinos η_ν . When this step is completed, the full event can be reconstructed and the first main goal of this project will be fulfilled.

Expanding the Analysis

As soon as the full event is reconstructable, several expansions for deeper research are possible. Some possible ideas are listed below. Currently, it has not been decided which of the following investigations will be conducted.

6 Outlook

- Measurement and comparison of the inclusive and STXS differential cross-section.
- Further SM investigations are possible. The channel offers insight into several interesting parameters such as the top Yukawa coupling or Higgs decay branching ratios.
- Compare the usage of modern techniques to classical algorithms. The overall speed and performance gain due to using **SPA-Net** can be quantified. Furthermore, this comparison could also include estimations on power consumption and CO₂ emissions.

No investigation into the spin correlation of the $H \rightarrow WW^*$ substructure will be done. The targeted event topology is expected to contain high background contamination and thus, is not suited for such analysis.

Bibliography

- [1] S. Weinberg, *The quantum theory of fields*, Cambridge university press (1995)
- [2] T. Banks, *Modern quantum field theory: a concise introduction*, Cambridge University Press (2008)
- [3] L. D. Faddeev, *Gauge fields: an introduction to quantum theory*, CRC Press (2018)
- [4] M. Gell-Mann, *The Eightfold Way: A Theory of strong interaction symmetry*, California Institute of Technology (1961)
- [5] F. J. Ynduráin, *Quantum chromodynamics: an introduction to the theory of quarks and gluons*, Springer (2013)
- [6] T.L. Barklow, *Electroweak symmetry breaking and new physics at the TeV scale*, volume 16, World Scientific (1996)
- [7] A.I. Akhiezer and V.B. Berestetskii, *Quantum Electrodynamics*, volume 1, Techical information Service extension (1953)
- [8] W. Greiner and J. Reinhardt, *Quantum Electrodynamics*, Springer (2013)
- [9] A. Salam, *Weak and Electromagnetic Interactions*, Conf. Proc. C. **680519** (1968)
- [10] S. Weinberg, *A Model of Leptons*, Phys. Rev. Lett. **19** (1967)
- [11] C. Jarlskog, *Quantum flavour dynamics*, Phys. Scrs **24** (1981)
- [12] M. Antonelli et. al., *Flavor physics in the quark sector*, Physics Reports **494** (2010)
- [13] S. L. Glashow, *Partial Symmetries of Weak Interactions*, J. Phys. G. **22** (1961)
- [14] P. W. Higgs, *Broken Symmetries and the Masses of Gauge Bosons*, Phys. Rev. Lett. **13** (1964)
- [15] F. Englert and R. Brout, *Broken Symmetry and the Mass of Gauge Vector Mesons*, Phys. Rev. Lett. **13** (1964)

Bibliography

- [16] G. S. Guralnik, C. R. Hagen and T. W. B. Kibble, *Global Conservation Laws and Massless Particles*, Phys. Rev. Lett. **13** (1964)
- [17] T. Brauner, *Spontaneous symmetry breaking and Nambu–Goldstone bosons in quantum many-body systems*, Symmetry **2** (2010)
- [18] A. Beekman, L. Rademaker and J.V. Wezel, *An introduction to spontaneous symmetry breaking*, SciPost Physics Lecture Notes (2019)
- [19] B. Povh et. al, *Particles and nuclei*, Springer (1995)
- [20] P. Langacker, *The standard model and beyond*, Taylor & Francis (2017)
- [21] G.D. Mahan, *Many-particle physics*, Springer (2013)
- [22] F. Halzen and A.D. Martin, *Quark & Leptons: An introductory course in modern particle physics*, John Wiley & Sons (2008)
- [23] N. Cabibbo, *Unitary Symmetry and Leptonic Decays*, Phys. Rev. Lett. **10** (1963)
- [24] Particle Data Group, *Review of Particle Physics*, PTEP (2023)
- [25] CDF Collaboration, *Observation of top quark production in $\bar{p}p$ collisions*, Phys. Rev. Lett. (1995)
- [26] DØ Collaboration, *Observation of the top quark*, Phys. Rev. Lett. (1995)
- [27] ATLAS Collaboration, *Performance of b-Jet Identification in the ATLAS Experiment*, JINST **11(04)** (2016)
- [28] CMS Collaboration, *Identification of b-Quark Jets with the CMS Experiment*, JINST **8** (2013)
- [29] ATLAS Collaboration, *ATLAS b-jet identification performance and efficiency measurement with $t\bar{t}$ events in $p\bar{p}$ collisions at $\sqrt{s} = 13$ TeV*, Eur. Phys. J. C **79(11)** (2019)
- [30] L. Randall, *Higgs discovery: the power of empty space*, Random House (2012)
- [31] J.F. Gunion, *The Higgs hunter's guide*, CRC Press (2018)
- [32] ATLAS Collaboration, *Observation of a new particle in the search for the Standard Model Higgs boson with the ATLAS detector at the LHC*, Phys. Lett. B **716** (2012)

- [33] CMS Collaboration, *Observation of a New Boson at a Mass of 125 GeV with the CMS Experiment at the LHC*, Phys. Lett. B **716** (2012)
- [34] D. Griffiths, *Introduction to Elementary Particles*, John Wiley & Sons (2020)
- [35] SNO Collaboration, *Direct Evidence for Neutrino Flavor Transformation from Neutral-Current Interactions in the Sudbury Neutrino Observatory*, Phys. Rev. Lett. **89** (2002)
- [36] F. Suekane, *Neutrino oscillations: a practical guide to basics and applications*, volume 898, Springer (2015)
- [37] T. Kuo and J. Pantaleone, *Neutrino oscillations in matter*, Reviews of Modern Physics **61** (1989)
- [38] B.R. Holstein, *Graviton physics*, American Journal of physics **74** (2006)
- [39] T. Damour and A.M. Polyakov, *String theory and gravity*, General Relativity and Gravitation **26** (1994)
- [40] V. Trimble, *Existence and nature of dark matter in the universe*, Annu. Rev. Astronomy & Astrophysics **25** (1987)
- [41] M.E. Peskin, *Dark matter and particle physics*, J. Phys. Soc. Jpn **76** (2007)
- [42] F. Zwicky, *Die Rotverschiebung von extragalaktischen Nebeln*, Helv. Phys. Acta **6** (1933)
- [43] S. Weinberg, *The cosmological constant problem*, Reviews of modern physics **61** (1989)
- [44] N. Arkani-Hamed, S. Dimopoulos and G. Dvali, *The hierarchy problem and new dimensions at a millimeter*, Phys. Lett B **429** (1998)
- [45] P. Fayet and S. Ferrara, *Supersymmetry*, Physics Reports **32** (1977)
- [46] T. Clifton et. al, *Modified gravity and cosmology*, Physics Reports **513** (2012)
- [47] *LHC Machine*, JINST **3** (2008)
- [48] L. R. Evans, *The Large Hadron Collider (LHC)*, Eur. Phys. J. C **34** (2004)
- [49] R. Alemany-Fernandez et. al, *Operation and Configuration of the LHC in Run 1* (2013), URL <https://cds.cern.ch/record/1631030>

Bibliography

- [50] J. Wenninger, *Operation and Configuration of the LHC in Run 2* (2019), URL <https://cds.cern.ch/record/2668326>
- [51] S. F. et. al, *LHC Configuration and Operational Scenario for Run 3*, Technical report (2021), URL <https://cds.cern.ch/record/2790409>
- [52] ATLAS Collaboration, *The ATLAS experiment at the CERN large hadron collider*, JINST **3**(S08003) (2008)
- [53] ATLAS Collaboration, *ATLAS: Detector and physics performance technical design report. Volume 1* (1999)
- [54] ATLAS Collaboration, *ATLAS: Detector and physics performance technical design report. Volume 2* (1999)
- [55] ATLAS Collaboration, *ATLAS inner detector: Technical design report. Vol. 1* (1997)
- [56] ATLAS Collaboration, *ATLAS inner detector: Technical design report. Vol. 2* (1997)
- [57] ATLAS Collaboration, *Technical Design Report for the ATLAS Inner Tracker Pixel Detector* (2017)
- [58] ATLAS Collaboration, *Technical Design Report for the ATLAS Inner Tracker Strip Detector* (2017)
- [59] ATLAS Collaboration, *The ATLAS Transition Radiation Tracker (TRT) proportional drift tube: Design and performance*, JINST **3** (2008)
- [60] ATLAS Collaboration, *ATLAS Calorimeter: Run 2 performance and Phase-II upgrades*, PoS **EPS-HEP2017** (2017)
- [61] *ATLAS muon spectrometer: Technical design report* (1997)
- [62] ATLAS Collaboration, *Technical Design Report for the Phase-II Upgrade of the ATLAS Muon Spectrometer* (2022)
- [63] ATLAS Collaboration, *New Small Wheel Technical Design Report*, Technical report (2013)
- [64] ATLAS Collaboration, *ATLAS high-level trigger, data acquisition and controls: Technical design report* (2003)
- [65] ATLAS Collaboration, *ATLAS level-1 trigger: Technical Design Report* (1998)

Bibliography

- [66] CMS Collaboration, *The CMS Experiment at the CERN LHC*, JINST **3** (2008)
- [67] ALICE Collaboration, *The ALICE experiment at the CERN LHC*, JINST **3** (2008)
- [68] LHCb Collaboration, *The LHCb Detector at the LHC*, JINST **3** (2008)
- [69] A. Shmakov et al., *SPANet: Generalized permutationless set assignment for particle physics using symmetry preserving attention*, SciPost Phys. (2022)
- [70] F. Fabbri, J. Howarth and T. Maurin, *Isolating semi-leptonic $H \rightarrow WW^*$ decays for Bell inequality tests*, Eur. Phys. J. C (2024)